JAAS

Using multiple micro-analytical techniques for evaluating quantitative synchrotron-XRF elemental mapping of hydrothermal pyrite

Journal:	*Journal of Analytical Atomic Spectrometry*
Manuscript ID	JA-ART-03-2019-000083.R2
Article Type:	Paper
Date Submitted by the Author:	14-Jun-2019

Complete List of Authors:	Del Real Contreras, Irene; Cornell University, Earth and Atmospheric Sciences Smieska, Louisa; Cornell University High Energy Synchrotron Source, Thompson, John; Cornell University, Earth and Atmospheric Sciences Martinez, Camila; Cornell University, School of Integrative Plant Science Thomas, Jay; Syracuse University, Earth Sciences Layton-Matthews, Daniel; Queen's University, Geological Sciences and Geological Engineering

Using multiple micro-analytical techniques for evaluating quantitative synchrotron-XRF elemental mapping of hydrothermal pyrite

del Real, I.*(1), Smieska, L.(2), Thompson, J.F.H.(1), Martinez, C.(3), Thomas, J.(4), Layton-Matthews, D(5).

(1) *Department of Earth and Atmospheric Sciences, Cornell University, Snee Hall, Ithaca NY, 14853, USA*
(2) *Cornell High Energy Synchrotron Source, Cornell University, Ithaca, USA*
(3) *Section of Plant Biology, School of Integrative Plant Science, Cornell University, USA*
(4) *Department of Earth Sciences, Syracuse University, USA*
(5) *Department of Geological Sciences and Geological Engineering, Queen's University, Canada*

Keywords: Synchrotron-XRF, mineral elemental composition, LA-ICPMS, EPMA, elemental mapping of hydrothermal pyrite

Abstract

Pyrite (FeS_2) elemental composition can be used as an indicator for hydrothermal fluid evolution both in low and high temperature environments. Synchrotron scanning x-ray fluorescence is an efficient, non-destructive, imaging technique that can be used to map heterogeneous pyrite elemental composition with excellent spatial resolution. The accuracy of quantified synchrotron-XRF elemental mapping relative to other widely trusted analytical techniques has not been previously evaluated for geologically relevant minerals such as pyrite. This study used pyrite samples from the Candelaria-Punta del Cobre Iron Oxide Copper Gold (IOCG) district in northern Chile to asses synchrotron scanning XRF as both an imaging method and quantitative analytical tool for observing local variations in pyrite chemistry. The results were quantified relative to a well-characterized pyrite sample as a standard. In order to evaluate the reliability of synchrotron-XRF as a quantitative tool, relative to laser inductively coupled plasma mass spectrometry and electron probe micro analyses, all three analyses were completed on the same pyrite grains and statistical tests were performed comparing data for Co, Ni, As and Se from all three analytical techniques. An overall strong positive correlation between the data sets was observed. Accuracy

* corresponding author
E-mail address: id92@cornell.edu (Irene del Real)

and reliability of the quantitative synchrotron-XRF results are strongly dependent on careful data processing. In the case of pyrite, peak overlaps between Co, Fe and Cu ultimately required a multistep approach to define spatial distributions and then derive accurate Co concentrations. Initial, consistently high concentrations of Co in the synchrotron-XRF data, arising from FeKβ/CoKα peak overlap, were mitigated by fitting only the Co Kβ line. Our results indicate that synchrotron-XRF is a reliable tool for acquiring quantitative accurate chemical data from geological specimens.

Introduction

Elemental composition of minerals is an important tool used in a wide range of geological (igneous petrology, volcanology, economic geology, etc.) to constrain processes and conditions of formation. Traditional analytical techniques to determine mineral elemental composition include laser inductively coupled plasma mass spectrometry (LA-ICPMS), electron probe micro analysis (EPMA), scanning electron microscopy (SEM) and secondary ion mass spectrometry (SIMS), among others. While among all of the techniques there is a tradeoff among spot size, detection limit, and the extent of sample destruction[1,2,3]. In this research we focus on LA-ICPMS and EPMA as examples of commonly used techniques with complementary resolutions and detection limits. LA-ICPMS can generate chemical concentration maps of minerals with low detection limits (down to the ppb level[4]), but it is limited by being sample destructive and having a spot size typically between 15–75 μm. Furthermore, data acquisition protocols for LA-ICPMS often present a practical limitation by linking the size of the final dataset to available computer memory. EPMA has a small spot size (<2 μm) and is non-destructive, but requires long data acquisition times in order to obtain low detection limits (often more than ten minutes in order to reach detection limits

in the tends of ppm); this presents practical limits on data acquisition[5]. Synchrotron X-Ray Fluorescence (synchrotron-XRF) analysis has the potential to reconcile these tradeoffs, by providing a non-destructive quantitative measurement technique with low detection limits (single unit ppm's), accuracy over several orders of magnitude, macroscale scan areas, and a range of available spot size (sub-micron – tens of μm).

Even though synchrotron-XRF has been employed for decades as a quantitative or semiquantitative analytical tool[6], there are few studies that directly compare XRF-based quantification on geologically-relevant systems with other, better known and more widely trusted techniques[7,8,9]. Furthermore, the potential applications of synchrotron-XRF in elemental analysis of minerals, particularly in mapping elemental composition, have been greatly expanded by advances in detector and signal processing technology over the last ten to fifteen years[10,11,12]. Recent synchrotron-XRF studies employing a Maia detector array to perform elemental mapping have been able to quantitatively image elemental zoning in sulfides (ESI1) associated silicate alteration minerals to support mineral deposit studies[3,13,14]. Previous studies have compared quantitative results of synchrotron-XRF mapping with other analytical techniques in biological relevant samples (e.g. with EPMA[15], LA-ICPMS[16] or NanoSims[17]). However, no study has directly evaluated the quantitative results of synchrotron-XRF elemental mapping in comparison with other analytical techniques in naturally occurring minerals.

As part of a research program related to high temperature hydrothermal pyrite in the Candelaria-Punta del Cobre Iron Oxide Copper-Gold (IOCG) district in northern Chile, a series of pyrite grains were selected and analyzed using synchrotron-XRF, EPMA and LA-ICPMS. The primary objective was to map and quantify elemental variation in zoned pyrite grains. Hydrothermal pyrite

has been used in several studies as a proxy to characterize the composition of hydrothermal fluids and the environment of deposition in both low temperature[18,19] and high temperature systems[20,21]. Most studies have combined low detection limit techniques (LA-ICPMS or SIMS) with techniques with high spatial resolution (EPMA; eg.[20,21,22]).

In this study we present quantitative elemental maps acquired through synchrotron scanning XRF, using a well-characterized pyrite sample as a standard. Quantitative results were compared in terms of relative accuracy to analyses by LA-ICPMS and EPMA. Statistical comparison of quantitative elemental concentrations from all three techniques used on the same pyrite grains validate both our overall quantification and the accuracy of the synchrotron-XRF data. The methodology for validating our data set has the potential to be used for evaluating quantitative synchrotron-XRF mineral chemical mapping data for other minerals.

Experimental

Analytical techniques

Sample preparation.

Samples and pyrite grains were selected following optical microscopic evaluation of polished thin sections. Selected rock slices were cut and mounted in 25 mm diameter epoxy mounts and polished down to 60 nm roughness using colloidal silica at the rock preparation laboratory at Syracuse University. The total thickness of the samples varied from 8 – 10mm, while pyrite grains of interest extended approximately 1 – 4 mm below the surface of the sample. For pyrite (FeS_2), the attenuation length for 14.5 keV incident x-rays is on the order of a few tens of μm. In the context of synchrotron-XRF analysis, these samples would be considered infinitely thick[23]. The same

epoxy mounts were used for all three analytical techniques (synchrotron-XRF, EPMA, and LA-ICPMS). Full sample descriptions, including main components and collection locations are listed in the electronic supplemental material, Table ESI1.

Standard preparation and characterization

There is no commercial pyrite standard available up to date; therefore, a well-characterized, highly homogenous natural pyrite sample from Los Colorados iron apatite deposit in Northern Chile was used as a standard for quantifying synchrotron-XRF measurements (sample CX-15). The pyrite standard sample is composed of several identical pyrite grains in a single epoxy mount and its standard analysis and characterization described in the next few paragraphs was performed by Martin Reich (pers. comm).

The pyrite standard has been extensively evaluated with micro-textural homogeneity confirmed using SEM, no chemical zonation was exhibited under back-scattered electron (BSE) analysis, and no evidence for textural heterogeneities such as pores, micro-inclusions, micro-fractures or micro-veins. Elemental mapping of the standard grains was performed using a JEOL JXA8530F electron microprobe (EMP) equipped with 5 wavelength dispersive spectrometers at the University of Western Australia in Crawley, Australia. Additionally, EMP point analysis and transects were undertaken in selected grains. Operational conditions were 40° take-off angle and beam energy of 20 keV. The beam current was 50 nA and the beam was fully focused (beam 1 μm). EMP data showed that major (Fe,S) and minor (Co, Ni, As) elements are homogenously distributed in the pyrite grains, with no significant chemical zonations or discontinuities.

SIMS analyses and elemental distribution maps of standard pyrite grains were performed at the Advanced Mineral Technology Laboratories (AMTEL) in London, Ontario, using a Cameca IMS-3f ion microprobe. The major sulfide-matrix constituent isotopes ^{56}Fe and ^{34}S were monitored, as well as the following ions: ^{63}Cu, ^{65}Cu, ^{75}As, ^{78}Se, ^{80}Se, ^{107}Ag, ^{121}Sb, ^{132}Sb, ^{128}Te. ^{130}Te and ^{197}Au. A 10 kV and 8 nA primary Cs^+ beam source was used for measurements, with a 4.5 kV accelerating voltage used for the negative secondary ions. The analytical spot size of the primary beam was ~25 μm; depth of analysis was 3.5–7.0 μm.

Mineral standards used for SIMS calibration were produced experimentally by implanting a known dosage of the element of interest into the pyrite matrix using the Tandetron accelerator at the University of Western Ontario. SIMS analytical results show that the trace elements analyzed are homogeneously distributed throughout the pyrite grains, and no nanoparticles or clusters or particles were detected during depth profiling.

For the pyrite standard, elemental concentrations measured using SIMS can be found in supplemental material Table ESI2 and elemental concentrations measured using EMP can be found in supplemental material Table ESI3.

Synchrotron-XRF mapping

Synchrotron-XRF mapping was performed at beamline F3 at the Cornell High Energy Synchrotron Source (CHESS). Station F3 was fed by a bending magnet and a double-multilayer monochromator was employed to select the energy of the X-rays. A 14.5 keV incident X-ray energy was selected for these scans. An ion chamber was used to monitor the incident x-ray intensity during measurements. To capture the maximum possible flux in a small spot, the X-ray

beam was focused with a unique single-bounce monocapillary to a 20 μm spot 55 m in front of the capillary tip[24,25]. A beamstop was placed upstream of the capillary to block X-rays at the center of the beam that would not be reflected by the capillary walls.

For scanning XRF measurements, samples and standards were mounted in a slide holder with the polished side unobscured, and placed at 45 degrees facing towards the incident beam. A four-element silicon detector (Vortex ME4) with a Quantum Xpress3 digital signal processor were employed to collect the XRF signal. Two layers of 0.0015" aluminum vacuum foil were placed between the sample and the detector to attenuate the strong iron fluorescence signal from the pyrite grains in the sample. The foil also attenuated peak signals near iron, which was acceptable for these geological specimens because the concentrations of the elements of interest were all relatively high. The addition of the Al foil to the XRF signal path helped to decrease the detector dead time but did not cause the measurement to become count rate limited. The pyrite standard (CX-15) was measured under the same conditions to account for the presence of the Al foil in the synchrotron-XRF calibration. Under typical scan conditions of 20 μm steps and 500 milliseconds dwell time per pixel, typical signals reached >250 kcps per channel with dead time <10%.

XRF data were processed using the open source Praxes software package developed at CHESS[26]. Praxes employs PyMCA libraries, developed at the European Synchrotron Research Facilities (ESRF) and widely used for XRF data processing, for spectra fitting and quantitative analysis[27]. XRF is a full-spectral technique, meaning that signal is simultaneously collected from all elements that fluoresce under the experimental conditions. Elements do not have to be pre-selected, and can be added to the fitting model as they are identified. Among its many features, PyMCA includes algorithms which model the spectrum background, make adjustments to peak shape, optimize peak

position, and account for sum peaks, escape peaks, and peak overlap[27]. Peak overlap in particular is largely accounted for by modelling XRF emission as groups of lines of known relative size[27]. This approach works well for a large range of cases, but as our data demonstrate, fitting artifacts can still arise when major and minor peaks coincide. PyMCA spectrum fitting is based on a nonlinear least-squares Levenberg-Marquardt algorithm [27]. When fitting numerous spectra in an imaging experiment, the speed of the analysis can be increased dramatically by fitting the nonlinear parameters, and then fixing them at constant values, and reducing the spectrum fitting to a linear least-squares problem. This strategy was employed in Praxes via PyMCA, and is also employed in other XRF fitting software[28].

For infinitely thick samples, the measured XRF signal for a given element at a given location depends on the local concentration of that element[23]. In PyMCA, the peak areas for a given element at a given location can be described as:

$$A = I_0 C \frac{\Omega}{4\pi} \Sigma_j R_j^{"}$$

Where A is the peak area, I_0 is the incident photon count, C is the mass fraction of the element at the given location, $\Omega/4\pi$ is the geometric detector efficiency (solid angle of collection), and $\Sigma_j R_j$" is the sum of the relative XRF emission lines for the element of interest, taking into account an absorption correction term which includes all layers between the sample surface and the detector, as well as adjustments to the expected intensities baser on a user-generated composition[27].

In our experiments, peak areas A and incident flux I_0 were measured and $\Sigma_j R_j$" was calculated in PyMCA[27], with a model that included the sample-detector air path and the aluminum foil filter, and the sample approximated as 0.5 mm pure pyrite. Therefore, to solve for the unknown mass

fraction C, only the detector efficiency was required. To quantify the scanning XRF data for the pyrites, the custom-made pyrite standard sample (sample CX-15) was scanned first and only once. The proportionality factor between ion chamber counts and incident flux which describes the detector efficiency (labeled "monitor efficiency" in Praxes) was adjusted to yield concentrations that matched the standard. This same detector efficiency term was then applied in the analysis of to the subsequently collected pyrite datasets, yielding quantified concentrations.

Once fitted and quantified, the elemental concentration data were exported as text files from Praxes. A different text file was generated for each element analyzed in a sample, containing all the concentration data of the correspondent 2D matrix. The XRF concentration data was further processed through the open source Anaconda software package using Python 2.7.12[29]. The first step of data processing consisted of isolating pyrite grains of interest from the area scanned by the synchrotron-XRF. This was done using Fe concentration, where pixels that contained between 44.5–47% Fe were defined as pyrite (Fig. 1A). The range of Fe defined as pyrite was calculated based on the trace element concentrations of Co and Ni (which replace Fe[30]) observed in the samples during reconnaissance EPMA analyses completed prior to the synchrotron-XRF program. Once the pixels were isolated and masked, the surrounding background was deleted, leaving only pixels containing pyrite (Fig. 1B). An interactive "Lasso" function from the Matplotlib package in Python[31] was used to exclude grains that were not analyzed with EPMA and LA-ICPMS The remaining pixels were used for the box plots and statistical tests shown in this study. (e.g. Fig. 2). Figure 2 shows an example of grain filtering; pixels in Figure 2B marked in red that contain low Co and variable As and were not used in the comparison analysis. Pixels in Figure 2B marked in blue have low As and variable Co and were used in this study. The exercise of masking pixels was

done by filtering the data in excel once the elemental concentration thresholds for excluded pixels were established.

EPMA

Point data was acquired on transects across pyrite grains in order to define representative values for heterogenous or zoned crystals. Samples were carbon coated before being analyzed to ensure conduction of the bean electrons away from the sample. Transects of 10–15 points analyses across grains were completed for each sample (Fig. 3). A Cameca SXFive electron microprobe at Syracuse University was used for trace element measurements and imaging of minerals. All imaging and quantitative measurements were performed with 15 kV accelerating voltage. For quantitative measurements, the five wavelength dispersive spectrometers were tuned, and elements were standardized using silicate, oxide and metal standard materials by adjusting the beam current to attain ~12,000 counts per second for analyte X-rays on gas-flow proportional counters. Measurements of unknowns were performed using a 200 nA beam current and a 2 μm beam diameter. Detailed wavelength dispersive scans were performed across the range of each spectrometer so that each point in a spectrum represented total peak time to identify elements present and to fully characterize spectral regions near measured X-ray positions. Total counts on X-ray peaks were determined by fitting a straight line to background positions on either side of peaks selected from wavelength dispersive spectra. Counts on each background were determined by peak time/2 with spectral positions selected to avoid any interferences (e.g. analyte Kβ X-rays, X-ray and lines from other interfering elements). Elements were acquired using the following analyzing crystals: LIF for Fe Kα, Co Kα, Ni Kα, As Kα and Se Kα. Counting time was 100 s for Ni Kα, As Lα, Se Lα and Co Kα, and 20 s (10 s in two spectrometers) for Fe Kα. Quantitative

EPMA X-ray spectrometry involves measurement of characteristic X-ray peak intensities corrected for background, therefore detection limits are controlled by the precision of background measurements. Numerous measurements of a chemically homogenous pyrite crystal were aggregated to improve precision of counts on the background positions, and detection limits were calculated as 3s above background counts at each X-ray position.

LA-ICPMS

Similar to EPMA, point data was acquired on transects across pyrite grains in order to assess heterogenous or zoned grains (Fig.3). Transects were designed to follow those analyzed by EPMA, although the samples were re-polished for in-situ sulfur isotope data acquirement (not presented in this study) and subsequent LA-ICPMS analysis, which removed the surface that was analyzed by EPMA. LA-ICPMS analyses were carried out at the Queen's University Facility for Isotope Research (QFIR) using a XSeries 2 ICP-MS coupled to a New Wave/ESI Excimer 193-nm laser ablation system. The LA-ICPMS calibration was initiated by analyzing a USGS glass standard (GSD) to optimize He and Ar flow through the ablation cell and the plasma torch. Point data was obtained using a beam diameter of 75 μm at a repetition rate of 10 Hz, with a gas blank of 10–20 s. The laser beam was focused on to the surface of the sample and the ICP-MS instrumentation was used to determine trace element concentrations in the ablated material. Analyses were bracketed by calibrations using USGS glass standards (GSC-1G, GSD-1G and GSE-1G) and external standards (BHVO-1, MASS-1 and NIST612) to monitor instrument drift and correct for elemental bias and laser yield. Raw data were plotted against the element calibration curves created using USGS glass standards to quantify the ablated areas. Data were collected in time-resolved graphics mode to monitor possible compositional heterogeneities that might be present in the

sample at the scale of the laser sampling and to monitor the inter-elemental fractionation that can occur during laser ablation analysis. The software package PlasmaLab was used for selecting and monitoring the data integration space of each point and element analyzed. The LA-ICPMS measured isotopes used for this study were ^{59}Co, ^{60}Ni, ^{75}As and ^{77}Se.

Statistical tests for analytical technique comparisons

Results for Co, Ni, As and Se were selected for the statistical tests comparing the three analytical techniques, as all four of these elements are common trace elements that occur within the pyrite structure, especially in IOCG deposits[21]. Co^{+2} and Ni^{+2} can substitute for Fe^{+2}, and As^{-1} and Se^{-1} can substitute for S^{-1} in pyrite[30,32]. Based on previous research on elemental compositions of pyrite from IOCG or IOA deposits (e.g. Mantoverde in Chile, Ernest Henry in Australia and Los Colorados in Chile[21,33,34]), the range of analytes expected was hundreds of ppm to a few wt.% for Co, Ni and As and a few 10's to hundreds of ppm for Se.

Results from EPMA and LA-ICPMS were compared prior to statistical tests between all three analytical techniques. Areas of the pyrite grains with concentrations of Co and/or Ni between 500-2000 ppm were selected, and the results from EPMA and LA-ICPMS were compared to assure both data sets were in agreement (less than 10% difference). Results from the data sets varied between 2%–10%, which is well within the variation attributed to the heterogenous nature of the pyrite grains, especially considering that each method analyzed a slightly different spot within the pyrite grains.

Detection limits of EPMA and values of the LA-ICPMS outside-standard calibration precluded the study from running statistical tests that compared the three techniques simultaneously on all

four elements. The number of data points for the LA-ICPMS and EPMA dataset are orders of magnitude lower than the synchrotron-XRF data set (Table 1). To visually compare the data sets, boxplots using the GGplot2 R package[35] were made for each element. The central box represents 50% of data from quartile 1 (Q1) to quartile 3 (Q3), and an outlier circle indicates the data that is further than 1.5 (Q3-Q1) from the box. The whiskers include the extreme outlier values. A logarithmic scaled boxplot was used as samples can have orders of magnitude differences in elemental concentration.

All statistical tests were conducted in R 3.5.1[36] software package. Normality tests for all sets of data were performed using the Shapiro-Wilk normality test, conducted with the Stats R package[36]. Significance levels for comparisons for each sample from each element included in the analyses were evaluated using three tests. The Kruskal-Wallis test ('Stats' package from R) was used to compare the three analytical methods together (synchrotron-XRF , EPMA and LA-ICPMS) for Co, As and Ni. The Kruskal-Wallis test was selected as it is used for comparing three (or more) independent non-normal distributed groups or data sets, with an equal or unequal sample size, therefore overcoming the drastic difference between the data set size of the synchrotron-XRF compared to the EPMA and LA-ICPMS[37]. Additionally, the Kruskal-Wallis – post-hoc after Nemenyi[38] was performed (using the 'PMCMR' R package) for identifying which method was significantly different when the Kruskal-Wallis test indicated significant differences. Test descriptions and their purposes are described in Table 2. P-values >0.05 indicate that the methods were not significantly different. P-values <0.01 indicate that methods are not similar (very significant). Intermediate p-values between 0.05 and 0.01 indicate that methods give similar results but still have some significant variation.

Even though the statistical tests performed should in principle not be affected by the difference in number of data points, a potential size effect has been observed in other studies[39]. In order to overcome this limitation we also performed statistical tests using pixels from the synchrotron-XRF following the same transects on the pyrite grain analyzed by EPMA and LA-ICPMS. The number of synchrotron-XRF data points selected by using pixels from transects is at least ten times less than the number of points across the whole grain (Table 1). The boxplots comparing the three data sets are included, providing a graphic tool to contrast and compare the analytical results. Statistical tests were run comparing: (1) whole pyrite grains analyzed with synchrotron-XRF with EPMA and LA-ICPMS, and (2) synchrotron-XRF transects on the pyrite grain analyzed by EPMA and LA-ICPMS. For all results of statistical tests shown throughout this study, samples tagged with * display non-significant differences between analytical methods, samples tagged with † display significant differences between analytical methods, and samples tagged with ÷ display very significant differences between analytical methods when statistical tests were run.

Results and discussion

Analytical technique comparison results

All results for non-normal data statistical tests with synchrotron-XRF performed on whole pyrite grains are presented in Table 3. All results for non-normal data statistical tests with synchrotron-XRF performed on pyrite grain transects are presented in Table 4. Statistical tests results using the synchrotron-XRF data set on whole pyrite grains and pyrite grain transects are the same, indicating that the statistical tests used for comparing the data from the different analytical methods were not skewed by the large number of points in the synchrotron-XRF datasets.

Variation in Se measurements

The Se data set is composed only of measurements taken with the LA-ICPMS and the synchrotron-XRF, as Se measurements taken with the EPMA are mostly below the detection limit. Boxplots comparing Se concentrations estimated with the synchrotron-XRF and the LA-ICPMS datasets indicate relatively similar results (Fig. 4). In most samples, the mean values are similar, within 10–20 ppm.

Variation in As measurements

The As dataset from all three analytical techniques was used to compare results (Fig. 5). Boxplots show tightly clustered mean values for samples AD0093-14, ES032-15 and ES032-5. Data from the synchrotron-XRF has the largest range, with EPMA and LA-ICPMS results falling within its numerical range, apart from sample DH996-23, where the LA-ICPMS data set has higher values.

Variation in Ni measurements

The Ni datasets from all three analytical techniques were analyzed (Fig. 6). Boxplots show tightly clustered mean values for samples AD0093-14 and DH996-2. Similar to the As results, Ni data from the synchrotron-XRF has the largest range, with EPMA and LA-ICPMS results falling within this numerical range.

Variation in Co measurements

The Co dataset includes most of the results from all three analytical techniques, with the exception of samples AD0093-14 and DH996-2. The Co concentration in these two samples are in average > 1%, therefore outside-standard calibration values of the LA-ICPMS. In synchrotron-XRF Kα and Kß peaks for each element are usually fit together as a single unit when analyzing XRF spectra,

to take advantage of known Kα-Kß peak ratios[27]. Fit in this manner, initial concentrations of Co from synchrotron-XRF were consistently higher than either EPMA or LA-ICPMS (Supplemental material Fig. ESI1). We attribute this overestimation to the overlap of the Co Kα peak with the extremely large Fe Kß peak in pyrite grains[40] (Fig. 7). Since pyrite contains ~46.55% Fe, the measured Fe signal in the synchrotron-XRF data is very high (both Kα and Kß; Fig. 7). To address this issue, we fit the Co Kß peak separately, allowing it to vary independently of the Co Kα peak (i.e., only the Co Kß peak was considered for determining Co concentration). After this fit adjustment, the Co concentration measured with synchrotron-XRF in the pyrite grains decreased considerably, yielding values similar to those of the EPMA and LA-ICPMS analytical techniques. Statistical tests on the Co Kß data set and a revised set of boxplots were compiled (Fig. 8; Table 3 and 4), representing the best-possible quantification of Co using synchrotron-XRF data.

This approach of fitting the Kα and Kß peaks separately has the benefit of decoupling the Co concentration from the Fe signal; however, the Co Kß peak does overlap with the Cu Kα peak, which can lead to false positive identification of Co in areas of high Cu concentration. In the samples examined for this study, the Co-Cu interference was only an issue in presence of the high-Cu mineral, chalcopyrite. As seen in the elemental maps: “false positive” Co signals arising from chalcopyrite are evident as red spots in Figure 8B, samples DH996-21, DH996-23, ES032-15, and LD1493-9. Chalcopyrite grains were easily excluded from statistical comparison of pyrite trace element concentrations, as shown in Figure 2.

Discussion

Analysis of pyrite samples using LA-ICPMS, EPMA and synchrotron-XRF show that each technique can be effective as a tool for mapping mineral chemical variations in the selected pyrite grains. The novelty of this extensive dataset is to show that synchrotron-XRF quantitative concentrations agree with results from more commonly used analytical techniques (e.g. EPMA and LA-ICPMS). Thus synchrotron-XRF offers a reliable tool for generating accurate chemical element maps based on thousands of spectral measurements, with time scales of acquisition, spatial resolution, and large scan areas that complement the capabilities of other mapping tools such as EPMA and LA-ICPMS.

Quantified synchrotron-XRF data

Quantitative synchrotron-XRF data has overall positive correlations with both LA-ICPMS and EPMA data. The use of statistical tests clarified the leading differences between the measurements methods while also considering the heterogenous nature of the pyrite grains and spot sizes of the different analytical methods.

Strongly heterogenous pyrites, i.e., complexly and finely zoned pyrites (e.g. DH996-2: Figs 4, 5, 6 and 7) or grains composed of aggregates of smaller pyrite crystals (e.g. DH996-21; Figs 4, 5, 6 and 7), tend to have p-values <0.05 when comparing datasets among the different analytical techniques, indicating significant differences between the measurement techniques (Table 3). The more heterogenous grains would require a larger dataset from EPMA and the LA-ICPMS in order to overcome heterogeneity and produce representative analytical data. Although the spot size for synchrotron-XRF is relatively small, the nature of the comprehensive spatial data may include fine-scaled heterogeneity or inclusions with anomalous concentrations that may be missed by the other more selective analytical techniques. This difference may explain the extended range of the

elemental data from the synchrotron-XRF for the elements considered in this study. Results from EPMA and LA-ICPMS techniques fall within the range of the synchrotron-XRF data, suggesting that the significant to very significant differences results obtained by the statistical tests reflect the variability in the number of data points acquired among the techniques, rather than an analytical error in one or more of the techniques. Dramatically reducing the number of points in the synchrotron-XRF dataset by selecting only transects for statistical tests does not reduce the extended range of the synchrotron-XRF data set relative to the other analytical techniques.

The spot size of the analysis may therefore also account for statistical differences between analytical techniques, as a spot size of 20 μm for was used for synchrotron-XRF, a spot size of 75 μm for LA-ICPMS, and a spot size of 2 μm for EPMA. Larger spot sizes may detect more local heterogeneity within the pyrite grains, and could unintentionally probe inclusions of other minerals that will introduce additional variability and error. The fine spot size of EPMA measurements agreed more closely with synchrotron-XRF measurements, displaying higher p-values in statistical tests, whereas statistical tests run between LA-ICPMS and synchrotron-XRF tend to have lower p-values, potentially reflecting the averaging of heterogeneities by the LA-ICPMS due to its larger spot size.

Cobalt concentrations and XRF data validation

When fitting the synchrotron-XRF Co Kα-Kß peaks as a unit, all cobalt p-values were < 0.05 when running statistical tests comparing the three different analytical techniques (Supplemental material Table ESI4), and synchrotron-XRF results were consistently higher. Separating the Co K peak fitting helped to improve the accuracy of the data set. The Co Kß peak does not overlap with Fe Kα peak (Fig. 7), resulting in a data set that behaves statistically in the same way as other elements

measured using the synchrotron-XRF and other techniques in this study. This approach has the advantage of not needing additional corrections and it can be done obtained directly during synchrotron-XRF spectral analysis. The Co Kß peak does, however, overlap with the Cu Kα peak[26], and thus use of the Co Kß peak as the primary means of determining Co concentrations may be compromised in Cu-rich samples (e.g. if the sample contains chalcopyrite inclusions or another Cu-rich sulfide mineral). Although this case was not encountered in these samples, it could be possible for both the Kα and Kß peaks of a minor element to suffer from overlap with major elements. To address this concern, we explored the possibility of using EPMA to generate a correction factor for the full synchrotron-XRF Co peak fitting, which is described in the supplemental material.

Synchrotron-XRF measurements can be quantified by analyzing an internationally validated reference material as standard (e.g. NIST, MASS-1, etc) but availability of such standards does not assure that all the resulting XRF data will be accurate. As shown in this study with Co and Fe, the accuracy of the concentration for some of the elements measured can largely depend on peak overlaps with other elements present in the material that is being analyzed, and it is up to the user to carefully validate the XRF spectral fits. Furthermore, if there is no validated standard reference material of the mineral being analyzed (as is the case with pyrite), a custom-made standard that reproduces the major elemtn matrix of the unknowns and that can be well characterized by other methods (e.g. LA-ICPMS) or a statistical comparison of the data set with other analytical techniques will be required to produce and verify accurate data.

Synchrotron-XRF vs EPMA vs LA-ICPMS

Among all of these analytical techniques there is a tradeoff between spot size, acquisition time and sensitivity, and in our analysis of pyrite grains the comparison between the synchrotron-XRF, EPMA and LA-ICPMS performance was no exception. The advantages and drawbacks of each technique are summarized in Table 5 and are discussed below.

LA-ICPMS performed well with elements with concentrations typically <10,000 ppm. Samples containing higher concentrations over-ranged (saturated the LA-ICPMS detector), which in this particular case can be attributed to calibration using standards that did not contain enough Co, Ni or As to bracket higher concentrations in some pyrite grains. The EPMA performed well at high concentrations, but suffered at low concentrations due to detection limits being higher than for the LA-ICPMS or the synchrotron-XRF techniques. Adding background measurements to the EPMA protocol will help to determine an accurate baseline, where the number of counts above the baseline can be better measured, hence significantly lowering detection limits[41,42]. EPMA measurements can have detection limits below 10s of ppm for some trace elements (e.g. Ni and Co), but are higher for other elements such as Se. The time for an analysis varies from ~1 minute/spot for LA-ICPMS to ~10 minutes/spot for EPMA, making the latter technique more time consuming when collecting multiple analyses on single grains. The EPMA dwell time can be reduced for elemental mapping, albeit on much smaller spatial scales and with much longer scan times[43] compared to other analytical techniques. EPMA is, however, non-destructive, and hence the sample can be used for other analyses without any major changes. LA-ICPMS is destructive[1], leaving pits on the analyzed surface that cannot be reanalyzed and requiring additional polishing of the sample for further analysis.

Synchrotron-XRF has several disadvantages, including: (1) lighter elements (lighter than Ar) produce lower energy XRF, which for the lightest elements is strongly absorbed by air in the path between the sample and the detector; (2) X-ray sample penetration is higher in EPMA and LA-ICPMS (10s of μm to a few mm, depending strongly on the sample matrix composition), requiring samples to be thicker than a regular thin section or mounted on quartz glass (regular float glass used for thin sections contains trace element impurities[14]); (3) quantified values for some elements can reflect peaks overlaps with other elements that are present in high concentrations (e.g. as demonstrated in this study by Co and Fe in pyrite), and must be carefully validated; and, (4) the number of synchrotron facilities is limited, particularly when compared to facilities for EPMA or LA-ICPMS.

Synchrotron-XRF, however, also offers complementary capabilities to EPMA and LA-ICPMS, including a substantially larger amount of data. Only a single standard measurement was needed for quantifying all the acquired data, and drifting of the machine is measured and corrected during quantification. The synchrotron-XRF produced detection limits near the ppb level for most elements, without causing problems in analyzing elements with major element concentrations (e.g. Fe in pyrite; Fig. 1A). Synchrotron-XRF is faster than LA-ICPMS and EPMA, taking on the order of a few to hundreds of milliseconds/spot and can run continuously for hours as necessary, enabling the study of larger samples sizes (tens of mm to tens of cm). While access to beamtime may be limited, significant volumes of data can still be acquired in that time. In addition, laboratory-based scanning XRF systems are becoming more widely accessible, although synchrotron-XRF retains the advantage of tunable incident energy, which can improve sensitivity to elements of interest. As with EPMA, synchrotron-XRF is non-destructive, leaving the sample intact for further analyses by other techniques. The resulting accuracy and scale of the geochemical data set that can be

obtained by synchrotron-XRF provides a powerful tool for investigating numerous geological, metallurgical and material questions with minimal sample preparation.

Conclusions

This research has verified the accuracy of quantified synchrotron-XRF chemical concentration measurements in hydrothermal pyrite using a custom made standard. Results of statistical tests show overall positive correlation when comparing synchrotron-XRF trace element data sets with EPMA and LA-ICPMS, although in some cases statistical tests showed differences between results obtained using the three techniques. These differences are attributed to the heterogenous nature of some of the pyrite grains (especially zoned pyrite grains) and the analytical instrument spot size, which varies between method.

The successful comparison between analytical techniques demonstrates that the synchrotron-XRF is an accurate and powerful analytical method that can be used to investigate mineral elemental composition. Synchrotron-XRF offers complementary capabilities to EPMA and LA-ICPMS, and provides data sets that are orders of magnitude larger than these more conventional techniques. The values of performing Synchrotron-XRF scans is that this method offers quantitative, rapid access to elemental distributions at both low and high concentrations across large areas, which neither of the other techniques can offer independently. Further comparative analytical tests using other mineral systems and other synchrotron facilities would be valuable to generalize our observations.

Acknowledgments

We would like to acknowledge Lundin Mining for funding field support and analytical results. We thank Martin Reich of University of Chile for providing the in-house standard use during this research. We thank the support of the staff of the Cornell High Energy Synchrotron Source (Rong Huang), Syracuse University EPMA laboratory (William Nachlas) and the Queens Facility for Isotope Research (Alexandre Voinot). Finally, Deniz Akdemir from Cornell Statistical Consulting Unit is thanked for the advice and help running the statistical tests used during this research. This work is based upon research conducted at the Cornell High Energy Synchrotron Source (CHESS) which is supported by the National Science Foundarion under award DMR-1332208.

References

1 M.A. Pearce, Godel, L.M. Fisher, L.A., Schoneveld, L.E., Cleverley, J.S., Oliver, N.H.S., M. Nugus, *Geological Society, London*, 2018, Special Publications, **453**, 7–39. DOI:10.1144/SP453.3

2 M. Reich, R. Large, A.P. Deditius, *Ore Geo. Rev*., 2017, **81**, 1215–1217. DOI:10.1016/j.oregeorev.2016.10.020

3 J.M. Stromberg, L.L. Van Loon, R. Gordon, A. Woll, R. Feng, D. Schumann, N.R. Banerjee, *Ore Geo. Rev*, 2018, **104**, 589–602. DOI:10.1016/J.OREGEOREV.2018.11.015

4 K.E. Jarvis, J.G. Williams, *Chem. Geo.*, 1993, **106**, 251–262. https://doi.org/10.1016/0009-254(93)90030-M

5 C. Hombourger, M. Outrequin, *Microscopy Today*, 2013, **21**, 10-15. DOI:10.1017/S15519295513000515

6 Janssens, K., De Nolf, W., Van Der Snickt, G., Vincze, L., Vekemans, B., Terzano, R., Brenker, F.E., 2010. TrAC Trends Anal. Chem. **29**, 464–478. doi:10.1016/J.TRAC.2010.03.003

7 Hahn, M., Behrens, H., Tegge-Schüring, A., Koepke, J., Horn, I., Rickers, K., Falkenberg, G., Wiedenbeck, M., 2005. Eur. J. Mineral. **17**, 233–242. doi:10.1127/0935-1221/2005/0017-0233

8 Phedorin, M.A., Bobrov, V.A., Chebykin, E.P., Goldberg, E.L., Melgunov, M.S., Filippova, S. V., Zolotarev, K. V., 2000. Geostand. Geoanalytical Res. **24**, 205–216. doi:10.1111/j.1751-908X.2000.tb00772.x

9 Zhang, C., Lin, J., Pan, Y., Feng, R., Almeev, R.R., Holtz, F., 2017. Geostand. Geoanalytical Res. **41**, 449–457. doi:10.1111/ggr.12169

10 Bordessoule, M., Fonda, E., Guignot, N., Itie, J.P., Menneglier, C., Orsini, F., 2019. AIP Conference Proceedings. AIP Publishing LLC , p. 060070. doi:10.1063/1.5084701

11 Lombi, E., de Jonge, M.D., Donner, E., Ryan, C.G., Paterson, D., 2011. Anal. Bioanal. Chem. **400**, 1637–1644. doi:10.1007/s00216-011-4829-2

12 West, M., Ellis, A.T., Streli, C., Vanhoof, C., Wobrauschek, P., 2017. J. Anal. At. Spectrom. **32**, 1629–1649. doi:10.1039/C7JA90035J

13 L.A. Fisher, D. Fougerouse, J.S. Cleverley, C.G. Ryan, S. Micklethwaite, A. Halfpenny, R.M. Hough, M. Gee, D. Paterson, D.L. Howard, K. Spiers, *Mineralium Deposita*, 2015, **50**, 665–674. DOI:10.1007/s00126-014-0562-z

14 J.M. Stromberg, E. Barr, L.L. Van Loon, R.A. Gordon, N.R. Banerjee, *Ore Geo. Rev.*, 2018, **104**, 603–619. DOI:10.1016/J.OREGEOREV.2018.11.020

15 Lerouge, C., Claret, F., Denecke, M.A., Wille, G., Falkenberg, G., Ramboz, C., Beny, C., Giffaut, E., Schäfer, T., Gaucher, E.C., Tournassat, C., 2010. Phys. Chem. Earth, Parts A/B/C **35**, 271–277. doi:10.1016/J.PCE.2010.04.003

16 Gholap, D.S., Izmer, A., De Samber, B., van Elteren, J.T., Šelih, V.S., Evens, R., De

Schamphelaere, K., Janssen, C., Balcaen, L., Lindemann, I., Vincze, L., Vanhaecke, F., 2010. Anal. Chim. Acta **664**, 19–26. doi:10.1016/J.ACA.2010.01.052

17 Moore, K.L., Chen, Y., Van De Meene, A.M.L., Hughes, L., Liu, W., Geraki, T., Mosselmans, F., Mcgrath, S.P., Grovenor, C., Zhao, F.-J., Zhao, J., 2014. New Phytol. **201**, 104–115. doi:10.1111/nph.12497

18 D.D. Gregory, R.R. Large, J.A. Halpin, E.L. Baturina, T.W. Lyons, S. Wu, L. Danyushevsky, P.J. Sack, A. Chappaz, V. V. Maslennikov, S.W. Bull, *Econ. Geo.,* 2015, **110**, 1389–1410. DOI:10.2113/econgeo.110.6.1389

19 R.R. Large, L. Danyushevsky, C. Hollit, V. Maslennikov, S. Meffre, S. Gilbert, S. Bull, R. Scott, P. Emsbo, H. Thomas, B. Singh, J. Foster, *Econ. Geo.,* 2009, **104**, 635–668. DOI:10.2113/gsecongeo.104.5.635

20 M. Reich, A. Deditius, S. Chryssoulis, J.W. Li, C.-Q. Ma, M.A. Parada, F. Barra, F. Mittermayr, *Geoch. Cosmo. Acta*, 2013, **104**, p. 42–62. DOI:10.1016/J.GCA.2012.11.006

21 M. Reich, A. Simon, A. Deditius, F. Barra, S. Chryssoulis, *Econ. Geo.,* 2016, **111**, 743–761. DOI:10.2113/econgeo.111.3.743

22 Franchini, M., McFarlane, C., Maydagán, L., Reich, M., Lentz, D.R., Meinert, L., Bouhier, V., 2015. Ore Geol. Rev. **66**, 366–387. doi:10.1016/J.OREGEOREV.2014.10.022

23 Sitko, R., 2009. Spectrochim. Acta Part B At. Spectrosc. **64**, 1161–1172. doi:10.1016/j.sab.2009.09.005

24 R. Huang, D.H. Bilderback, K. Finkelstein, *Journal of Synch. Rad.,* 2014, **21**, 366–375. DOI:10.1107/S1600577514000514

25 R. Huang, D.H. Bilderback, *Journal of Synch. Rad.,* 2006, **13**, 74–84. DOI:10.1107/S0909049505038562

26 Dale, D., 2015. available at https://github.com/praxes/praxes

27 V.A. Solé, E. Papillon, M. Cotte, P. Walter, J. Susini, *Spectrochim. Acta - Part B Atomic Spec*., 2007, **62**, 63–68. DOI:10.1016/j.sab.2006.12.002

28 Alfeld, M., Janssens, K., 2015. J. Anal. At. Spectrom. **30**, 777–789. doi:10.1039/C4JA00387J

29 Python Softwarre Foundation, *Python Lamguage Reference,* 2010, version 2.7. Available at http://www.python.org

30 W.M. Temmerman, P.J. Durham, D.J. Vaughan, *Physics and Chem. of Min.*, 1993, **20**, 248–254. DOI:10.1007/BF00208138

31 J.D. Hunter, *Computing in Science and Engineering*, 2007, **9**, 90–95. DOI:10.1109/MCSE.2007.55

32 P.K. Abraitis, R.A.D. Pattrick, *Intern. Journal of Min. Proces.*, 2004, **74**, 41–59. DOI:10.1016/j.minpro.2003.09.002

33 Benavides, J., Kyser, T.K., Clark, A.H., Oates, C.J., Zamora, R., Tarnovschi, R., Castillo, B., 2007. Econ. Geol. **102**, 415–440. doi:10.2113/gsecongeo.102.3.415

34 Rusk, B., Oliver, N., Cleverley, J., Blenkinsop, T., Zhang, D., 2010. Hydrothermal iron oxide copper-gold and related deposits: A global perspective: Adelaide, PGC Publishing, **3**, 187-204.

35 V. Gómez-Rubio, *Journal of Stat. Soft.* 77, 2017, **1**, 1–3. DOI:10.18637/jss.v077.b02

36 R.D.C. Team, *R Foundation Statistical Computing*, 2017, **1**, 409. DOI:10.1007/978-3-540-74686-7

37 Landau, S., Everitt, B., 2004. A handbook of statistical analyses using SPSS.

38 T. Pohlert, *R package version,* 2018, DOI:10.18637/jss.v080.i01>

39 G.M. Sullivan, R. Feinn, *Journal of Grad. Med, Edu*., 2012, **4**, 279–282. DOI:10.4300/JGME-D-12-00156.1

40 A. Thompson, D. Atwwod, E. Gullikson, M. Howells, J. Kortright, A. Robinson, *X-ray data booklet,* 2009, URL http://xdb.lbl.gov

41 A. C. Dunham, F.C.F. Wilkinson, Albite, A., *X-Ray Spectr.*, 1978, **7**, 50–56.

42 C. Merlet, J.L. Bodinier, *Chem. Geo.*, 1990, **83**, 55–69. DOI:10.1016/0009-2541(90)90140-3

43 R. Holder, B. Hacker, *Chem. Geo.*, 2019, **504**, 35-52. DOI:10.1016/j.chemgeo.2018.11.017

Figures

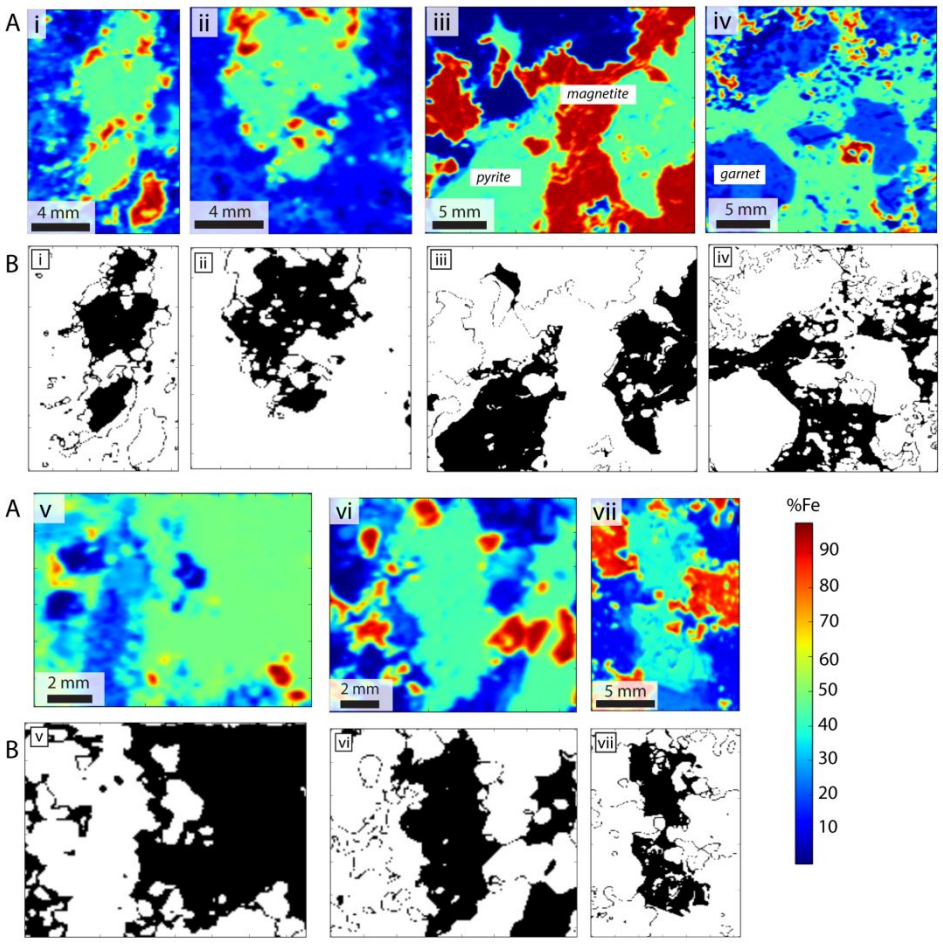

Figure 1: (A) Quantified synchrotron-XRF Fe maps, from blue (less Fe) to red (more Fe); pyrite grains are pale-green, magnetite grains are red to red-orange. The blue background minerals are silicates. (B) Depicted in black are the masked pyrite pixels/data points of samples using Fe contents of the same map displayed in (A). Samples are: (i) DH996-2; (ii) DH996-23; (iii) DH996-21; (iv) ES032-5; (v) ES032-15; (vi) AD0093-14 and; (vii) LD1493-9.

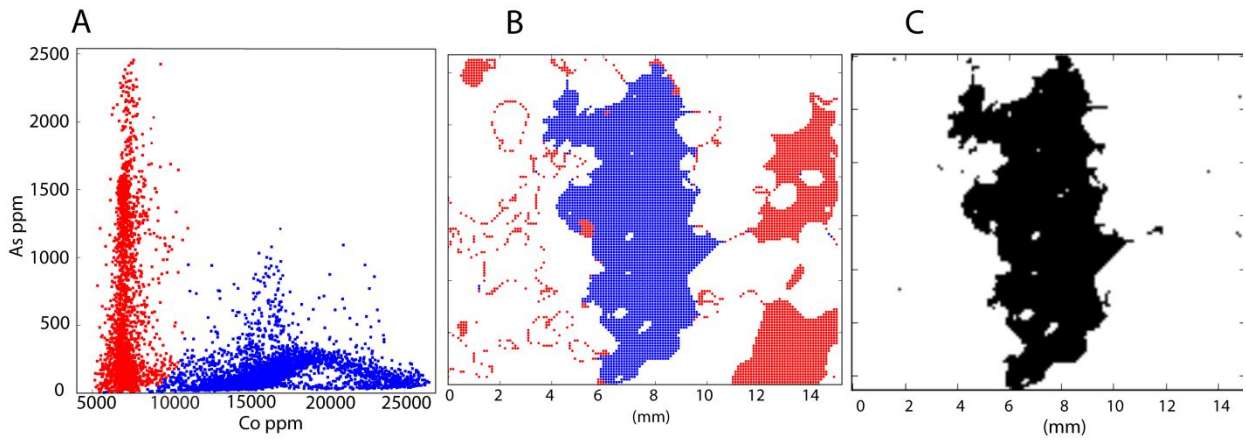

Figure 2: Identification of pyrite grains with different element concentrations. Element variation plots using Co and As (A) were used to identify spatial variation of pyrites (B) with distinctive trace elements. The vertical axis scale on the pyrite map is the same as in the horizontal scale. Figure (C) represents the pixels that were used for the study, after masking pixels with low Co and variable As.

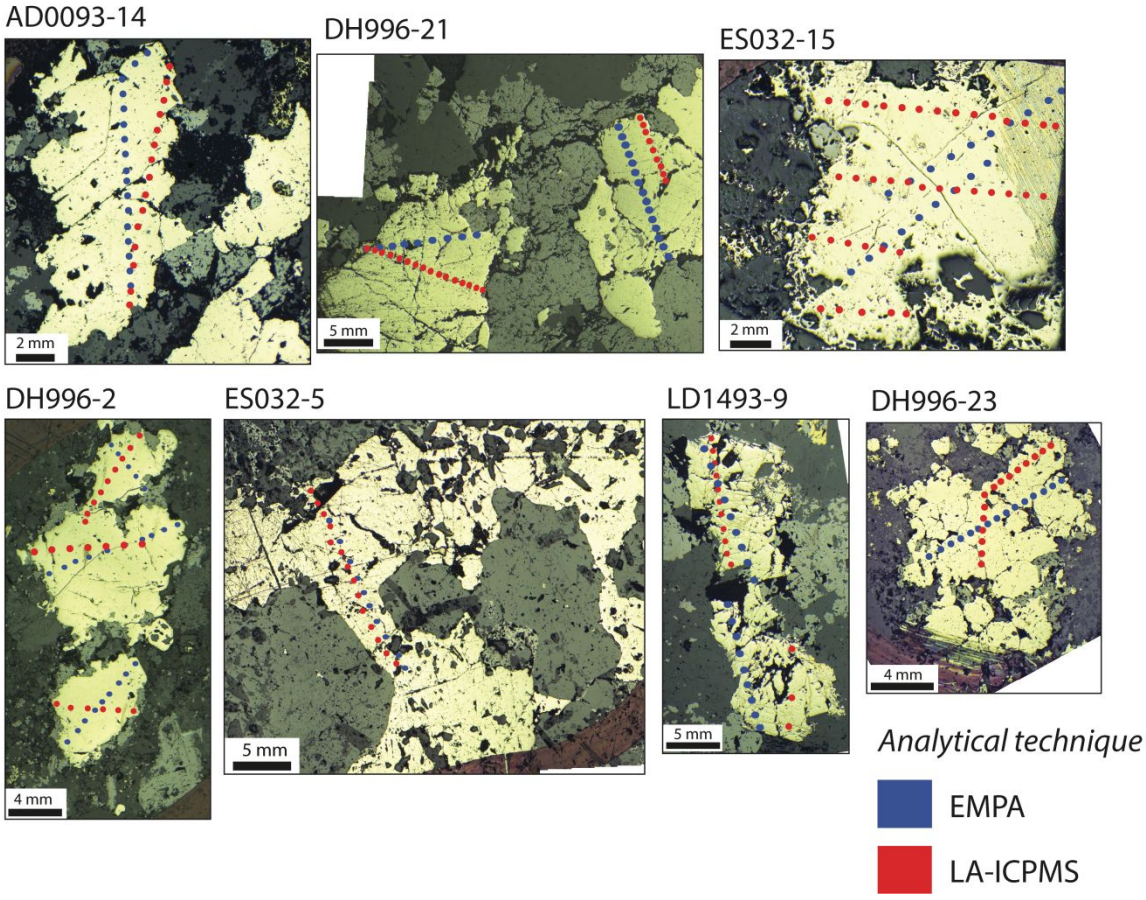

Figure 3: Reflected light photos of pyrite grains used for this study indicating the spots that were analyzed with LA-ICPMS (red) and EMPA (blue)

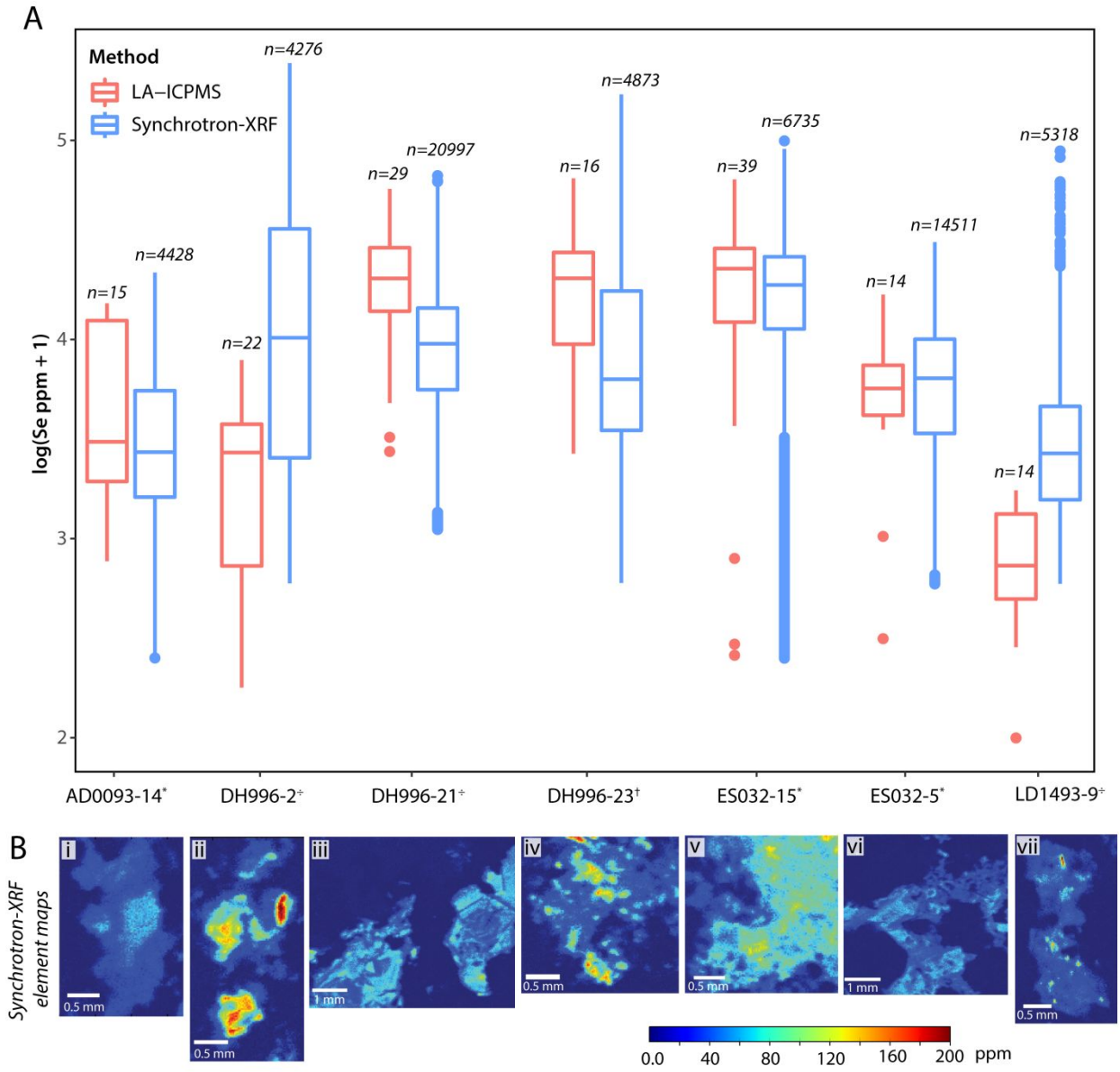

Figure 4: (A) Boxplots for Se data comparing synchrotron-XRF and LA-ICPMS measurements. (B) synchrotron-XRF quantified element maps for Se. Samples are: (i) AD0093-14; (ii) DH996-2; (iii) DH996-21; (iv) DH996-23; (v) ES032-15; (vi) ES032-5; (vii) LD1493-9.

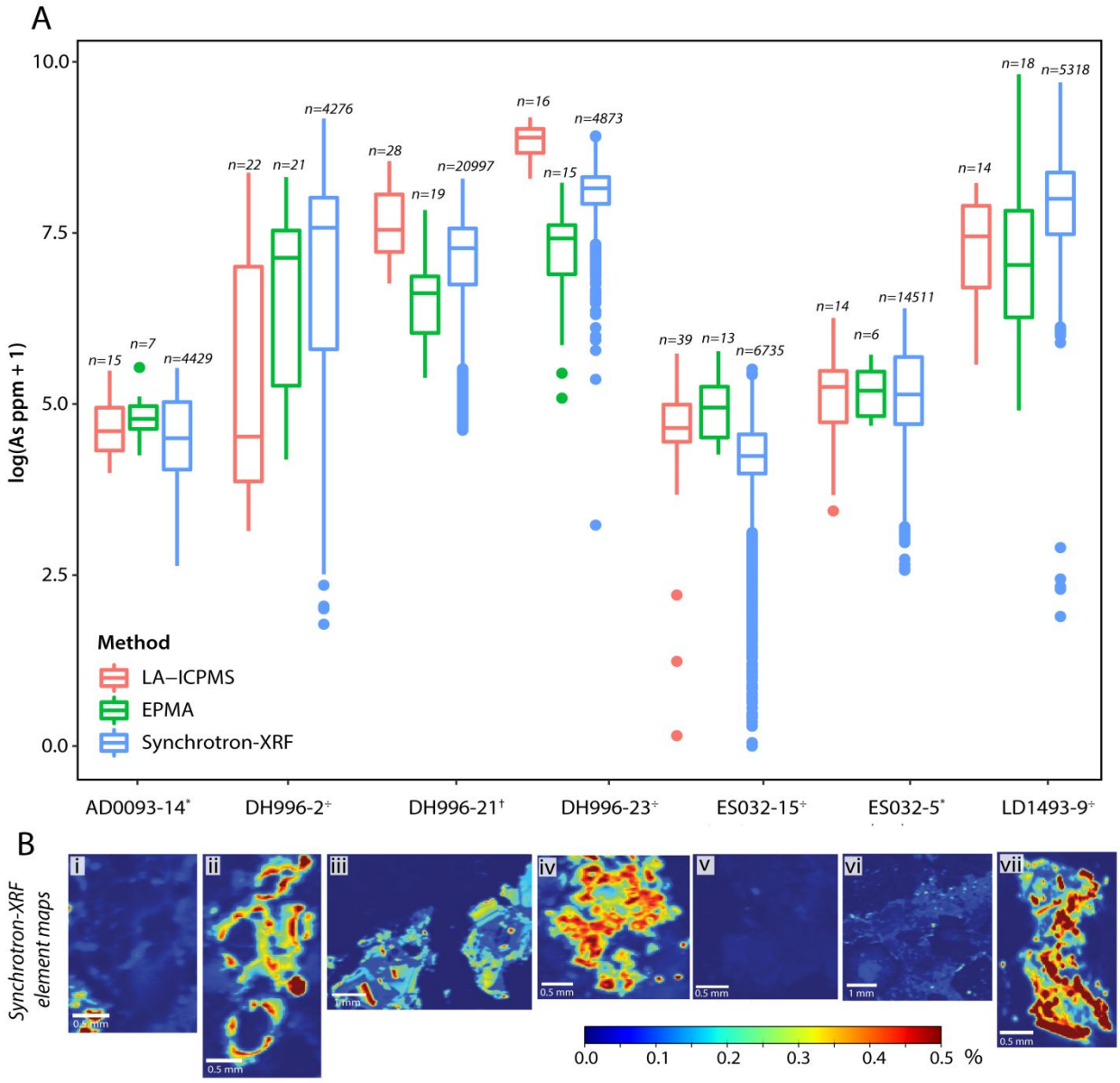

Figure 5: (A) Boxplots for As data comparing synchrotron-XRF, EPMA and LA-ICPMS measurements. (B) synchrotron-XRF quantified element maps for As. Samples are: (i) AD0093-14; (ii) DH996-2; (iii) DH996-21; (iv) DH996-23; (v) ES032-15; (vi) ES032-5; (vii) LD1493-9.

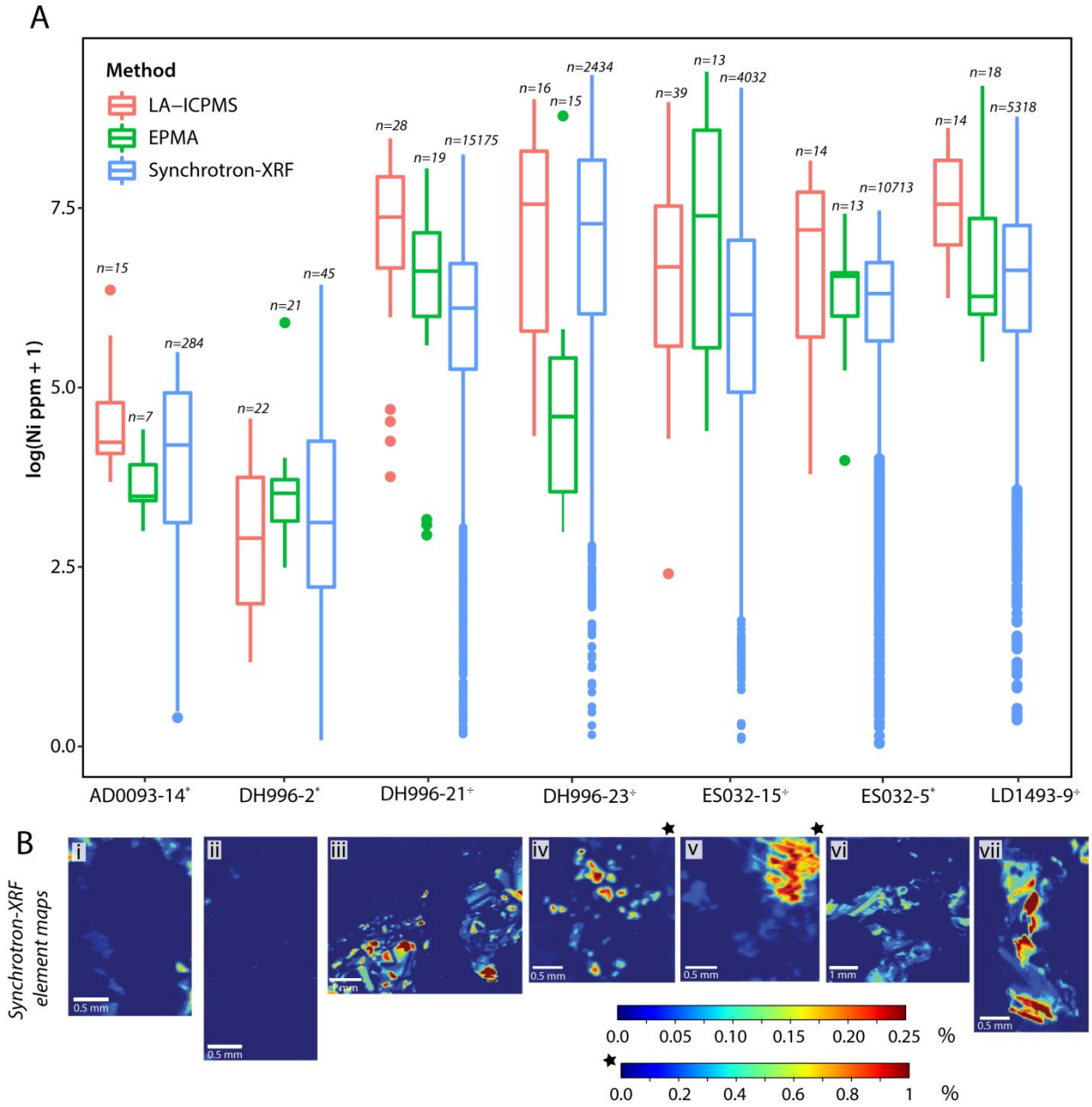

Figure 6: (A) Boxplots for Ni data comparing synchrotron-XRF, EPMA and LA-ICPMS measurements. (B) synchrotron-XRF quantified element maps for Ni. Samples are: (i) AD0093-14; (ii) DH996-2; (iii) DH996-21; (iv) DH996-23; (v) ES032-15; (vi) ES032-5; (vii) LD1493-9.

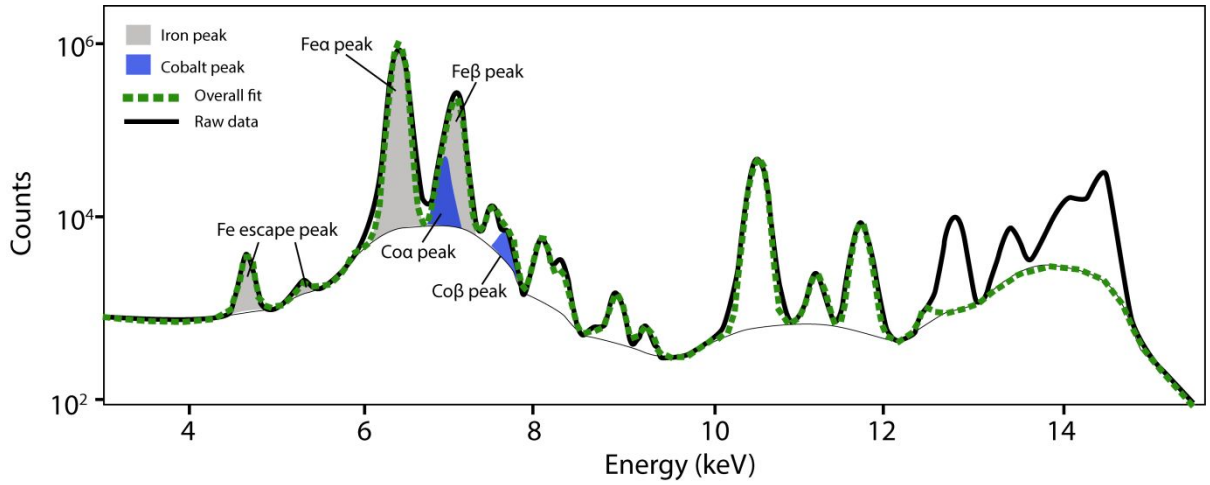

Figure 7: Synchrotron-XRF energy spectra for sample DH996-2. The Kα Co peak (6.930 KeV) overlaps with Fe Kβ peak (7.057 KeV). The black thick line is the raw data and in green is the overall fit for the spectra obtained. The two lower Fe peaks in the spectra are escape peaks (Fe minus the energy of silicon, an artifact arising from the high count rate on the silicon detector).

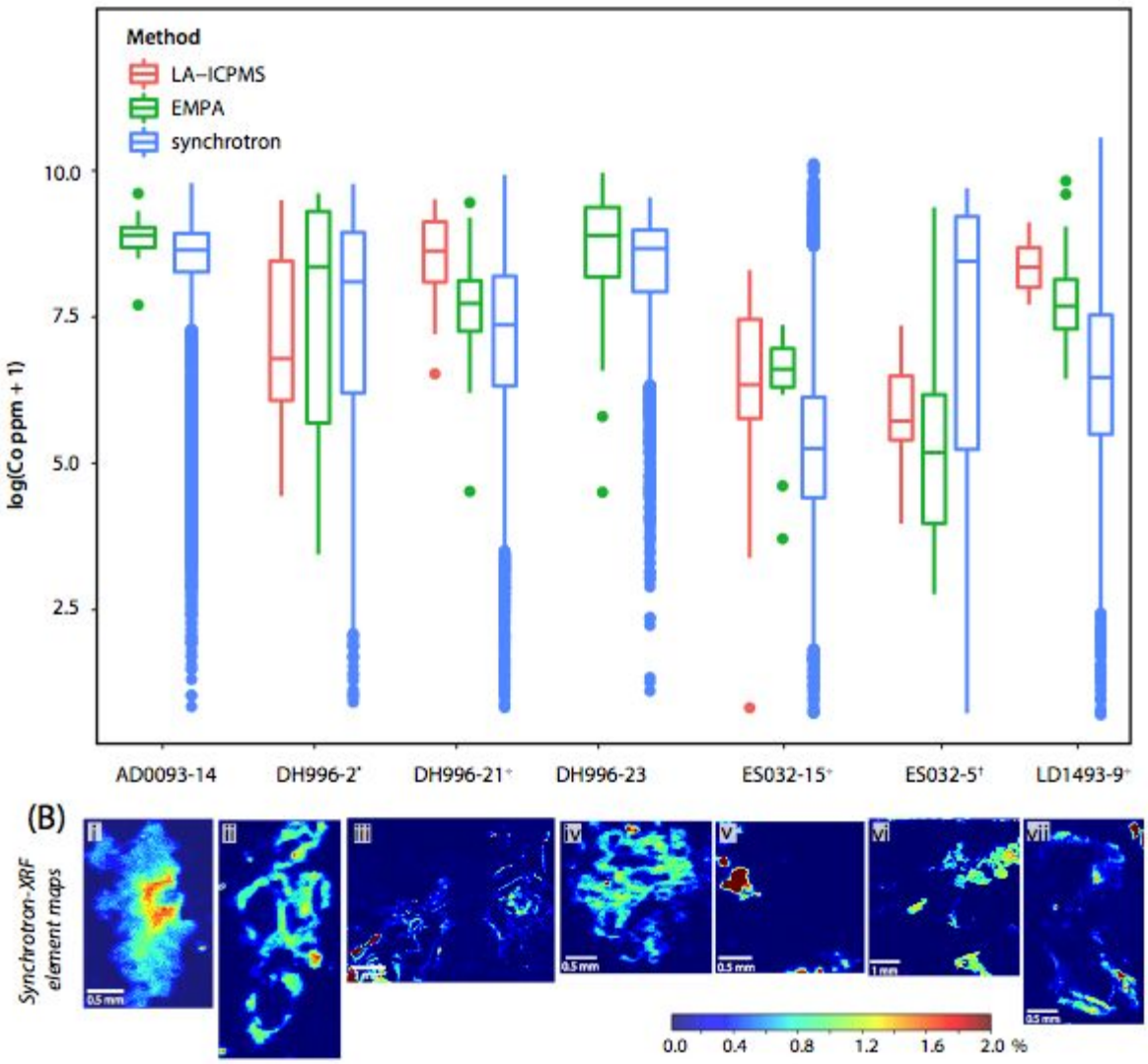

Figure 8: Boxplots with corrected Co data comparing synchrotron-XRF CoKβ peak, EPMA and LA-ICPMS measure \ments. (B) synchrotron-XRF quantified element maps for CoKβ. Samples are: (i) AD0093-14; (ii) DH996-2; (iii) DH996-21; (iv) DH996-23; (v) ES032-15; (vi) ES032-5; (vii) LD1493-9. Saturated areas outside the pyrite grains are due to CoKβ overlap with CuKα (chalcopyrite grains) were not part of the statistical tests.

Tables

Element	Sample	Number of point data			
		LA-ICPMS	Microprobe	Synchrotron-XRF	Synchrotron-XRf transect
Se	AD0093-14	15	-	4428	189
	DH996-2	22	-	4276	191
	DH996-21	29	-	20997	294
	DH996-23	16	-	4873	131
	ES032-15	39	-	6735	254
	ES032-5	14	-	14511	114
	LD1493-9	14	-	5318	135
As	AD0093-14	15	7	4428	189
	DH996-2	22	21	4276	191
	DH996-21	28	19	20997	294
	DH996-23	16	15	4873	131
	ES032-15	39	13	6735	254
	ES032-5	14	6	14511	114
	LD1493-9	14	18	5318	135
Ni	AD0093-14	15	7	284	150
	DH996-2	22	9	45	15
	DH996-21	28	19	15175	215
	DH996-23	16	8	2434	75
	ES032-15	29	19	4032	254
	ES032-5	14	9	10713	114
	LD1493-9	14	20	4840	135
Co	AD0093-14	2	15	4428	189
	DH996-2	20	25	4276	191
	DH996-21	20	23	20997	294
	DH996-23	1	15	4873	131
	ES032-15	38	17	6735	254
	ES032-5	11	10	14511	114
	LD1493-9	13	21	5318	135

Table 1: Number of data points for the synchrotron-XRF, LA-ICPMS and EMPA data sets.

Statistical Test	Purpose	Use
Shapiro-Wilk normality test	Checking if random samples come from a normal distribution.	Whole data set
Kruskal-Wallis rank sum test	Tests whether the mean ranks are the same in all the data sets. Used when the measurement variable does not meet the normality.	LA-ICPMS, EMPA and Synchrotron-XRF simultaneously
Kruskal-Wallis – post-hoc after Nemenyi	Calculates pairwise multiple comparisons between group levels. Sometimes referred to as Nemenyi-tests for multiple comparisons of (mean) rank sums of independent samples. Used when the measurement variable does not meet the normality. Used it for identyfying which method was significantly different when the Kruskal-Wallis test indicated significant differences	LA-ICPMS, EMPA and Synchrotron-XRF between each other
Wilcoxon rank sum test	Tests whether two samples are likely to derive from the same population (e.g., that the two populations have the same shape). Used when measurement variable does not meet the normality.	LA-ICPMS and Synchrotron-XRF

Table 2: Description and use of statistical tests completed on the synchrotron-XRF, EMPA and -LA-ICPMS data set.

Element	Sample	Test,synchrotron2XRF,whole,grain									
		Wilkoxon-rank-		Kruskal)Wallis		Posthoc.kruskal.nemenyi					
		Synchrotron) XRF-vs-LA) ICPMS		Synchrotron) XRF-vs-EMPA-vs-LA)ICPMS		Synchrotron) XRF-vs.-LA) ICPMS		Synchrotron) XRF-vs-EMPA		EMPA-vs.-LA) ICPMS	
Se	AD0093)14	0.3479	*	)		)		)		)	
	DH996)2	$1.5*10^{)6}$	÷	)		)		)		)	
	DH996)21	$2.6*10^{)7}$	÷	)		)		)		)	
	DH996)23	0.002964	÷	)		)		)		)	
	ES032)15	0.1572	*	)		)		)		)	
	ES032)5	0.8001	*	)		)		)		)	
	LD1493)9	0.00021	÷	)		)		)		)	
As	AD0093)14	)		0.254	*	0.63	*	0.35	*	0.81	
	DH996)2	)		0.0007289	÷	0.0014	÷	0.2872	*	0.3811	
	DH996)21	)		0.00000014	÷	0.00054	÷	0.000083	÷	$5.8*10^{)8}$	
	DH996)23	)		$8.7*10^{)16}$	÷	$1.8*10^{)10}$	÷	0.00000088	÷	$3.4*10^{)14}$	
	ES032)15	)		$1.2*10^{)9}$	÷	0.0000041	÷	0.00007	÷	0.45	
	ES032)5	)		0.993	*	0.99	*	1	*	1	
	LD1493)9	)		0.00000712	÷	0.02348	†	0.0038	÷	0.9017	
Ni	AD0093)14	)		0.198	*	0.35	*	0.52	*	0.2	
	DH996)2	)		0.343	*	0.61	*	0.67	*	0.33	
	DH996)21	)		0.0000021	÷	0.000005	÷	0.16	*	0.23	
	DH996)23	)		0.01307	†	0.999	*	0.024	†	0.0433	
	ES032)15	)		0.0103	†	0.248	*	0.012	†	0.439	
	ES032)5	)		0.06814	*	0.06	*	0.88	*	0.55	
	LD1493)9	)		0.00163	÷	0.0011	÷	0.9236	*	0.0338	
Co)Kß)	AD0093)14			)		)		0.35	*	)	
	DH996)2			0.3284	*	0.43	*	0.68	*	0.3	
	DH996)21			0.000000087	÷	0.0000013	÷	0.244	*	0.026	
	DH996)23			)		)		0.11	*	)	
	ES032)15			0.000000484	÷	0.00027	÷	0.005	÷	0.967	
	ES032)5			0.01655	†	0.095	*	0.043	†	0.95	
	LD1493)9			$1.9*10^{)9}$	÷	0.000091	÷	0.00005	÷	0.62	

Table 3: P-values for the statistical tests completed on the synchrotron-XRF, LA-ICPMS and EMPA data sets for Se, As, Ni, CoKß and corrected Co concentration data using whole pyrite grain synchrotron-XRF data.

Element	Sample	Test synchrotron-XRF transects				
		Wilkoxon rank	Kruskal-Wallis	Posthoc.kruskal.nemenyi		
		Synchrotron-XRF vs LA-ICPMS	Synchrotron-XRF vs EMPA vs LA-ICPMS	Synchrotron-XRF vs. LA-ICPMS	Synchrotron-XRF vs EMPA	EMPA vs. LA-ICPMS
Se	AD0093-14	0.8588 *	-	-	-	-
	DH996-2	0.000092 ÷	-	-	-	-
	DH996-21	$5.6*10^{-7}$ ÷	-	-	-	-
	DH996-23	0.000043 ÷	-	-	-	-
	ES032-15	0.0717 *	-	-	-	-
	ES032-5	0.019 †	-	-	-	-
	LD1493-9	0.00053 ÷	-	-	-	-
As	AD0093-14	-	0.711 *	0.69 *	1 *	0.87 *
	DH996-2	-	0.0373 †	0.028 †	0.99 *	0.181 *
	DH996-21	-	$5.5*10^{-11}$ ÷	$7.8*10^{-11}$ ÷	0.0876 *	0.0014 ÷
	DH996-23	-	$2.4*10^{-11}$ ÷	$4.5*10^{-9}$ ÷	0.011 †	1.1E-10 ÷
	ES032-15	-	0.000125 ÷	0.0105 †	0.0028 ÷	0.3672 *
	ES032-5	-	0.993 *	0.0062 ÷	0.0253 †	0.8926 *
	LD1493-9	-	0.000575 ÷	0.1001 *	0.0022 ÷	0.7907 *
Ni	AD0093-14	-	0.00586 ÷	0.0054 ÷	0.8224 *	0.0505 *
	DH996-2	-	0.173 *	0.95 *	0.17 *	0.19 *
	DH996-21	-	$6.3*10^{-7}$ ÷	0.0000007 ÷	0.026 †	0.298 *
	DH996-23	-	0.605 *	0.0011 ÷	0.8064 *	0.0187 †
	ES032-15	-	0.018 †	0.34 *	0.027 †	0.489 *
	ES032-5	-	0.04378 †	0.00052 ÷	0.54 *	0.99553 *
	LD1493-9	-	0.00122 ÷	0.0011 ÷	0.9236 *	0.0338 †
Co Kß	AD0093-14		-	-	0.19 *	-
	DH996-2		0.2965 *	1 *	0.973 *	0.54 *
	DH996-21		$1.2*10^{-8}$ ÷	0.19538 *	0.00023 ÷	0.2 *
	DH996-23		-	-	0.11 *	-
	ES032-15		$3.9*10^{-8}$ ÷	$1.6*10^{-11}$ ÷	0.0000024 ÷	0.98 *
	ES032-5		0.56675 *	0.95 *	0.54 *	0.98 *
	LD1493-9		0.0401 †	0.3245 *	0.1519 *	0.05 *

Table 4: P-values for the statistical tests completed on the synchrotron-XRF, LA-ICPMS and EMPA data sets for Se, As, Ni and CoKß using pyrite grain synchrotron-XRF transects.

Analytical technique	Advantages	Drawbacks
Synchrotron-XRF	• non-sample destructive • Spot size can be small (down to 1 µm) • Does not saturate with elements in higher concentration. • Provides substantially larger amounts of data • low detection limits	• Elements lighter than Ar are difficult to measure • X-ray sample penetration is higher, therefor thin sections in float glass cannot be used. • Peak overlap can distort quantified values, requiring data analysis and correction • The number of facilities are limited
EPMA	• non-sample destructive • Spot size is small (down to 1 µm) • Does not saturate with elements in higher concentration. • commonly available instrument	• Requires long data acquisition time on order to obtain low detection limits • Detection limits are higher than for the LA-ICPMS or synchrotron-XRF • Different elements require different standards
LA-ICPMS	• Detection limits are low • commonly available instrument • requires less data acquisition time for low detection limits	• Average spot size is larger • Can saturate or over-range for outside-standard calibration values • Data protocols present a practical limitation by linking the size of the final dataset to available memory of the instrument. • sample destructive analytical technique

Table 5: Advantages and drawbacks of synchrotron-XRF, EPMA and LA-ICPMS.